

RESEARCH ARTICLE

Towards a Material Point Method with C^1 -continuous Powell-Sabin spline basis functions on unstructured triangulations

Pascal de Koster | Roel Tielen | Elizaveta Wobbles | Matthias Möller

Department of Applied Mathematics, Section of Numerical Analysis, Delft University of Technology, Van Mourik Broekmanweg 6, 2628 XE Delft, The Netherlands

Correspondence

Pascal de Koster. Email: p.b.j.dekoster@tudelft.nl

Present Address

Delft University of Technology, Mekelweg 2, 2628 CD Delft, The Netherlands

Summary

Within the original Material Point Method (MPM), discontinuous gradients of the piece-wise linear basis functions lead to so-called ‘grid-crossing errors’ when particles cross element boundaries. This can be overcome by using C^1 -continuous basis functions such as higher-order B-splines. In this paper, we extend this approach to unstructured triangulations by using C^1 -continuous high-order Powell-Sabin (PS) spline basis functions. Numerical results, presented for a two-dimensional benchmark, show the potential of these basis functions within MPM.

KEYWORDS:

Material point method, B-splines, Powell-Sabin splines, grid-crossing error, higher-order convergence

1 | INTRODUCTION

The Material Point Method (MPM) has proven to be successful in solving complex engineering problems that involve large deformations, multi-phase interactions and history-dependent material behaviour. Over the years, MPM has been applied to a wide range of applications, including modelling of sea ice dynamics¹, pile driving² and the evolution of landslides³.

Within MPM, a continuum is discretised by defining a set of Lagrangian particles, called material points, which store all relevant material properties. An Eulerian background grid is adopted on which the equations of motion are solved in every time step. The solution on the background grid is then used to update all material point properties (e.g. displacement, velocity, stress). In this way, MPM avoids the numerical difficulties of nonlinear convective terms associated with an Eulerian problem formulation⁴, while grid distortion, typical for Lagrangian formulations, is prevented as well^{5,2}.

Classically, MPM makes use of piece-wise linear Lagrange basis functions, also known as ‘tent’ functions. However, the gradients of these basis functions are discontinuous at element boundaries, which leads to so-called grid-crossing errors^{6,7} when material points cross this discontinuity. Grid-crossing errors can significantly influence the quality of the numerical solution and may eventually lead to a lack of convergence^{8,9}.

Over the years, different methods have been developed to mitigate the effect of grid-crossings, like the Generalised Interpolation Material Point Method (GIMP)⁶ or the Dual Domain Material Point Method (DDMP)¹⁰. On structured rectangular grids, adopting C^1 -continuous B-spline basis functions completely removes grid-crossing errors^{7,11}. Additionally, these B-spline basis functions have shown to result in higher-order spatial convergence. However, a B-spline approach for unstructured triangular grids does not yet exist to the best of our knowledge.

In this paper, we present a spline-based variant of MPM for unstructured triangulations, that uses Powell-Sabin (PS) splines, which are C^1 -continuous and thereby overcome grid-crossing errors by design. Numerical results are presented for a two-dimensional benchmark and compared with an analytic solution. Furthermore, a spatial convergence study is performed, where a comparison is made with the standard MPM.

This paper is organised as follows. In Section 2, the governing equations are presented, and MPM is introduced to solve these equations. In Section 3, the construction of PS-spline basis functions and their application within MPM is described. In Section 4, numerical results of a two-dimensional benchmark on an unstructured triangulation are presented. In Section 5, conclusions and recommendation are given.

2 | MATERIAL POINT METHOD

We will summarise the MPM as introduced by Sulsky et al.⁵ to keep this work self-contained. First, the governing equations are presented, after which the MPM is introduced to solve these equations.

2.1 | Governing Equations

The deformation of a continuum is modelled using the conservation of momentum and a material model. It should be noted that MPM can be implemented with a variety of material models that either use the rate of deformation² or the deformation gradient. However, for this study it is sufficient to consider the simple Neo-Hookean model that is based on the gradient of the deformation. Using the Einstein summation convention, the system of equations in a Lagrangian frame of reference for each direction x_k is given by

$$\frac{\partial u_k}{\partial t} = v_k, \quad (1)$$

$$\rho \frac{\partial v_k}{\partial t} = \frac{\partial \sigma_{kl}}{\partial x_k} + \rho g_k, \quad (2)$$

$$D_{kl} = \delta_{kl} + \frac{\partial u_k}{\partial x_l}, \quad (3)$$

$$\sigma_{kl} = \frac{\lambda \ln(J)}{J} \delta_{kl} + \frac{\mu}{J} (D_{mk} D_{ml} - \delta_{kl}), \quad (4)$$

where u_k is the displacement, t is the time, v_k is the velocity, ρ is the density, g_k is the body force, D_{kl} is the deformation gradient, δ_{kl} is the Kronecker delta, σ_{kl} is the stress tensor, λ is the Lamé constant, J is the determinant of the deformation gradient, and μ is the shear modulus. Equation (2) describes the conservation of linear momentum and Equation (4) the material model for the Neo-Hookean solid.

Initial conditions are required for the displacement, velocity, and stress tensor. The boundary of the domain Ω can be divided into a part with a Dirichlet boundary condition for the displacement and one with a Neumann boundary condition for the traction:

$$u_k(\mathbf{x}, t) = U_k(\mathbf{x}, t) \quad \text{on } \partial\Omega_u(t), \quad (5)$$

$$\sigma_{kl}(\mathbf{x}, t) n_l = \tau_k(\mathbf{x}, t) \quad \text{on } \partial\Omega_\tau(t), \quad (6)$$

where $\mathbf{x} = [x_1 \ x_2]^T$ and \mathbf{n} is the unit vector normal to the boundary $\partial\Omega$ and pointing outwards.

For solving the equations of motion in the material point method, the conservation of linear momentum in Equation (2) is required in its weak form:

$$\int_{\Omega} \phi \rho a_k \, d\Omega = \int_{\Omega} \phi \frac{\partial \sigma_{kl}}{\partial x_k} \, d\Omega + \int_{\Omega} \phi \rho g_k \, d\Omega, \quad (7)$$

in which $a_k = \frac{\partial v_k}{\partial t}$ is the acceleration and ϕ is a continuous test function that satisfies the imposed Dirichlet boundary condition. After applying integration by parts, the Gauss integration theorem and splitting the boundary, the weak form can be rewritten as

$$\int_{\Omega} \phi \rho a_k \, d\Omega = \int_{\partial\Omega_\tau} \phi \tau_k \, dS - \int_{\Omega} \frac{\partial \phi}{\partial x_l} \sigma_{kl} \, d\Omega + \int_{\Omega} \phi \rho g_k \, d\Omega. \quad (8)$$

2.2 | Discretised Equations

Equation (8) can be solved using a finite element approach by defining n_{bf} basis functions ϕ_i ($i = 1, \dots, n_{bf}$). The acceleration field a_k is then discretised as a linear combination of these basis functions,

$$a_k(\mathbf{x}) = \sum_{j=1}^{n_{bf}} \hat{a}_{k,j} \phi_j(\mathbf{x}), \quad (9)$$

in which $\hat{a}_{k,j}$ is the j^{th} acceleration coefficient corresponding to basis function ϕ_j . Substituting Equation (9) into Equation (8) and replacing the test function by ϕ_i leads to

$$\int_{\Omega} \phi_i \rho \left(\sum_{j=1}^{n_{bf}} \hat{a}_{k,j} \phi_j \right) d\Omega = \int_{\partial\Omega_{\tau}} \phi_i \tau_k dS - \int_{\Omega} \frac{\partial \phi_i}{\partial x_l} \sigma_{kl} d\Omega + \int_{\Omega} \phi_i \rho g_k d\Omega, \quad \text{for } i = 1, \dots, n_{bf}. \quad (10)$$

By exchanging summation and integration, this can be rewritten in matrix-vector form,

$$\sum_{j=1}^{n_{bf}} \underbrace{\left(\int_{\Omega} \phi_i \rho \phi_j d\Omega \right)}_{M_{ij}} \hat{a}_{k,j} = \underbrace{\int_{\partial\Omega_{\tau}} \phi_i \tau_k dS}_{F_{k,i}^{trac}} - \underbrace{\int_{\Omega} \frac{\partial \phi_i}{\partial x_l} \sigma_{kl} d\Omega}_{F_{k,i}^{int}} + \underbrace{\int_{\Omega} \phi_i \rho g_k d\Omega}_{F_{k,i}^{body}}, \quad \text{for } i = 1, \dots, n_{bf}, \quad (11)$$

$$\Rightarrow \mathbf{M} \hat{\mathbf{a}}_k = \mathbf{F}_k^{trac} - \mathbf{F}_k^{int} + \mathbf{F}_k^{body}, \quad (12)$$

where \mathbf{M} denotes the mass matrix, $\hat{\mathbf{a}}_k$ the coefficient vector for the acceleration, while \mathbf{F}_k^{trac} , \mathbf{F}_k^{int} and \mathbf{F}_k^{body} denote respectively the traction, internal and body force vector in the x_k -direction. When density, stress and body force are known at time t , the coefficient vector $\hat{\mathbf{a}}_k$ can be solved from Equation (12). Using the acceleration field at time t , the properties of the continuum at time $t + \Delta t$ can then be determined.

2.3 | Material Point Method solution procedure

The discrete momentum equation can be solved over time using MPM, where we adopt the step-by-step procedure as presented in ². Within MPM, the continuum is discretised by a set of n_p particles, storing all physical properties. At each time step, the particle information is projected onto a background grid, on which the momentum equation is solved. Particle properties and positions are updated according to this solution, as illustrated in Figure 1

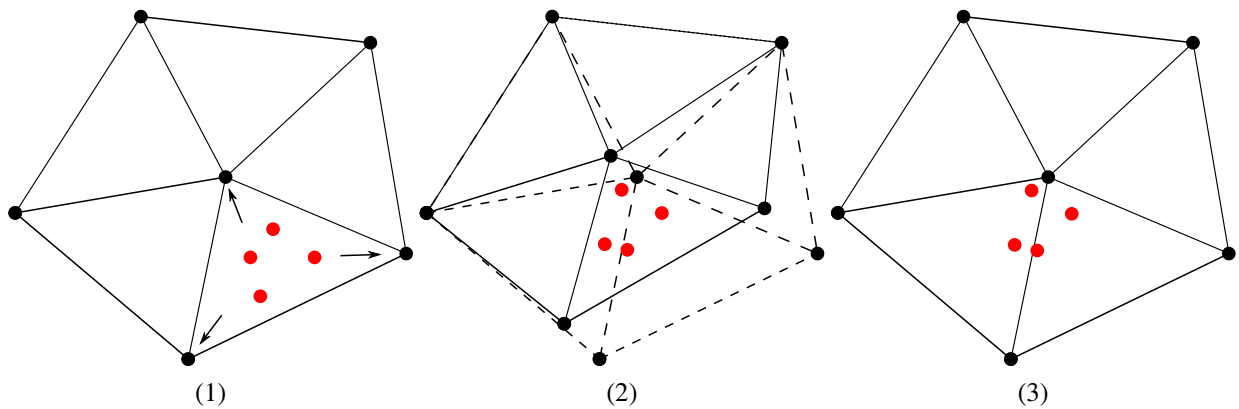


FIGURE 1 One time step in the MPM procedure. (1) Projection of particle properties onto the background grid. (2) Update of particle properties based on solution on the background grid. (3) Resetting the grid.

To solve Equation (12) at every time step of MPM, the integrals in Equation (11) have to be determined. Since the material properties are only known in the particles, the particle positions are used as integration points for numerical quadrature, and the

particle volumes V as integration weights. Let there be n_p particles, indexed p . This index is used as subscript for properties at that particle. A superscript t is also assigned to particle properties that change over time. The mass matrix and force vectors are then defined by

$$\mathbf{M}_{ij}^t = \sum_{p=1}^{n_p} V_p^t \rho_p^t \phi_i(\mathbf{x}_p^t) \phi_j(\mathbf{x}_p^t) = \sum_{p=1}^{n_p} m_p \phi_i(\mathbf{x}_p^t) \phi_j(\mathbf{x}_p^t), \quad (13)$$

$$\mathbf{F}_{k,i}^{trac,t} = \sum_{p=1}^{n_p} \phi_i(\mathbf{x}_p^t) f_{k,p}^{trac,t}, \quad (14)$$

$$\mathbf{F}_{k,i}^{int,t} = \sum_{p=1}^{n_p} V_p^t \frac{\partial \phi_i}{\partial x_m}(\mathbf{x}_p^t) \sigma_{mk,p}^t, \quad (15)$$

$$\mathbf{F}_{k,i}^{body,t} = \sum_{p=1}^{n_p} V_p^t \rho_p^t \phi_i(\mathbf{x}_p^t) g_k = \sum_{p=1}^{n_p} m_p \phi_i(\mathbf{x}_p^t) g_k, \quad (16)$$

in which m_p denotes the particle mass, which is set to remain constant over time, guaranteeing conservation of mass. The coefficient vector $\hat{\mathbf{a}}_k^t$ at time t for the x_k -direction is then determined by solving

$$\mathbf{M}^t \hat{\mathbf{a}}_k^t = \left(\mathbf{F}_k^{trac,t} - \mathbf{F}_k^{int,t} + \mathbf{F}_k^{body,t} \right). \quad (17)$$

The reconstructed acceleration field is then used to update the particle velocity:

$$v_{k,p}^{t+\Delta t} = v_{k,p}^t + \Delta t a_k^t(\mathbf{x}_p^t) = v_{k,p}^t + \Delta t \sum_{j=1}^{n_{bf}} \hat{a}_{k,j}^t \phi_j(\mathbf{x}_p^t). \quad (18)$$

The semi-implicit Euler-Cromer scheme¹² is then adopted to update the remaining particle properties. First, the velocity field $v_k^{t+\Delta t}$ is discretised as a linear combination of basis functions,

$$v_k^{t+\Delta t}(\mathbf{x}) = \sum_{j=1}^{n_{bf}} \hat{v}_{k,j}^{t+\Delta t} \phi_j(\mathbf{x}), \quad (19)$$

in which $\hat{\mathbf{v}}_k^{t+\Delta t}$ is the velocity coefficient vector for the velocity field at time $t + \Delta t$. The coefficient vector $\hat{\mathbf{v}}_k^{t+\Delta t}$ is then determined from a density weighted L_2 -projection onto the basis functions ϕ_i . This results in the following system of equations

$$\mathbf{M}^t \hat{\mathbf{v}}_k^{t+\Delta t} = \mathbf{P}_k^{t+\Delta t}, \quad (20)$$

where \mathbf{M}^t is the same mass matrix as defined in Equation (13). $\mathbf{P}_k^{t+\Delta t}$ denotes the momentum vector, of which the coefficients are given by

$$\mathbf{P}_{k,i}^{t+\Delta t} = \sum_{p=1}^{n_p} m_p v_{k,p}^{t+\Delta t} \phi_i(\mathbf{x}_p). \quad (21)$$

Particle properties are then updated in correspondence with Equations (1)-(4). First, the velocity gradients are calculated:

$$\nabla v_{kl,p}^{t+\Delta t} = \frac{1}{2} \sum_{j=1}^{n_{bf}} \left(\hat{v}_{k,j}^{t+\Delta t} \frac{\partial \phi_j}{\partial x_l}(\mathbf{x}_p^t) + \hat{v}_{l,j}^{t+\Delta t} \frac{\partial \phi_j}{\partial x_k}(\mathbf{x}_p^t) \right). \quad (22)$$

After that, the deformation gradients and its determinant are obtained:

$$\mathbf{D}_{kl,p}^{t+\Delta t} = \left(\delta_{kl} + \nabla v_{kl,p}^{t+\Delta t} \Delta t \right) \mathbf{D}_{kl,p}^t, \quad (23)$$

$$\mathbf{J}_p^{t+\Delta t} = \det(\mathbf{D}_p^{t+\Delta t}). \quad (24)$$

The particle stresses are then computed as follows:

$$\sigma_{kl,p}^{t+\Delta t} = \frac{\lambda \ln(\mathbf{J}_p^{t+\Delta t})}{\mathbf{J}_p^{t+\Delta t}} \delta_{kl} + \frac{\mu}{\mathbf{J}_p^{t+\Delta t}} \left(\mathbf{D}_{mk,p}^{t+\Delta t} \mathbf{D}_{ml,p}^{t+\Delta t} - \delta_{kl} \right). \quad (25)$$

The determinant of the deformation gradient is used to update the volume of each particle. The density is then updated such that the mass of each particle remains constant.

$$V_p^{t+\Delta t} = J_p^{t+\Delta t} V_p^0, \quad (26)$$

$$\rho_p^{t+\Delta t} = m_p / V_p^{t+\Delta t}. \quad (27)$$

Finally, particle positions and displacements are updated from the velocity field

$$x_{k,p}^{t+\Delta t} = x_{k,p}^t + \Delta t \sum_{i=1}^{n_{bf}} v_{k,i}^{t+\Delta t} \phi_i(\mathbf{x}_p^t), \quad (28)$$

$$u_{k,p}^{t+\Delta t} = u_{k,p}^t + \Delta t \sum_{i=1}^{n_{bf}} v_{k,i}^{t+\Delta t} \phi_i(\mathbf{x}_p^t). \quad (29)$$

The described MPM can be numerically implemented by performing the steps in Equations (13)-(29) in each time step in the shown order. This summarises the material point method used in this work, apart from the choice of basis functions ϕ_i , whose special choice will be discussed in the next section.

3 | POWELL-SABIN SPLINE BASIS FUNCTIONS

In this section, Powell-Sabin (PS) spline basis functions^{13,14} are considered, which are C^1 -continuous piece-wise quadratic splines defined on an unstructured triangulation. Furthermore, these PS-splines exhibit the partition of unity property and are non-negative over their entire support, which is local as in classical FEM. A preview of these basis functions can be found in Figure 8. For completeness of this work, the construction process of PS-splines is summarised here shortly from the work of Dierckx^{13,14}.

3.1 | Powell-Sabin grid refinement

To construct PS-splines, a triangulation Δ of a planar domain Ω has to be refined to a so-called Powell-Sabin refinement Δ^* ¹⁵. A possible refinement Δ^* is shown in Figure 2, which can be constructed in the following way:

1. For each triangle t_j , choose an interior point Z_j , such that if two triangles t_j and t_m have a common edge, the line between Z_j and Z_m intersects the edge. The intersection point is called Z_{jm} . A way to guarantee the existence of the point Z_{jm} is by choosing all Z_j as the incenter of its triangle t_j .
2. Connect all Z_j to the vertices of its triangle t_j with straight lines.
3. For each triangle t_j , connect the interior point Z_j to all edge points Z_{jm} with straight lines. In case t_j is a boundary element, connect Z_j to an arbitrary point on each boundary edge, for example the edge middle.

It is known that any C^1 -continuous function, that is piece-wise quadratic on the refined triangles of Δ^* , can be constructed as a linear combination of $3n_v$ Powell-Sabin basis functions, where n_v is the number of vertices in the original triangulation Δ ^{14,15}. The construction procedure that three basis functions are associated with each vertex and posses the properties of non-negativity and C^1 -continuity. Let the union of the unrefined triangles directly around V_i be called the *molecule* Ω_i , as shown as the grey area in Figure 2. Each basis function is locally defined around its associated vertex V_i and only non-zero inside its molecule Ω_i . At the molecule edge, the basis function smoothly vanishes to ensure C^1 -continuity. To construct PS-splines that posses these properties, first control triangles are created around each vertex. From the control triangles, the PS-splines are then created.

3.2 | Control Triangles

Control triangles are created to define suitable non-negative PS-splines. For each vertex V_i in the original triangulation Δ , a local set of PS-points PS_i is defined consisting of V_i and the midpoints of all edges in the PS-refinement Δ^* with V_i at one end, as shown with dots in Figure 3. To ensure non-negative basis functions, a control triangle is constructed containing all PS-points in PS_i . The control triangle is not uniquely defined, as shown in Figure 3. To produce PS-splines with good stability properties,

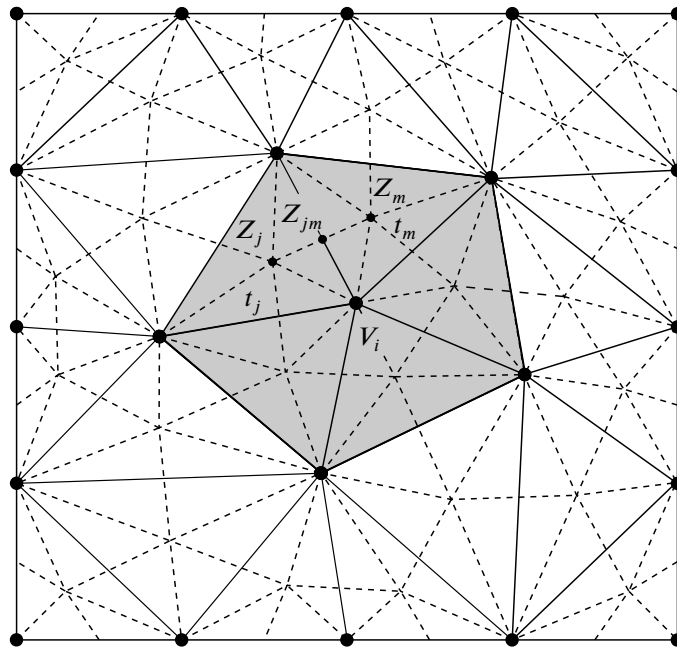


FIGURE 2 A PS-refinement Δ^* (solid and dashed lines) of a triangulation Δ (solid lines only). The molecule Ω_i around vertex V_i is marked grey.

the control triangle should have a small area¹⁶. A sufficiently good PS-triangle can be constructed by considering only control triangles with two or three edges shared with the convex hull of PS_i , as shown in Figure 3, and then taking the one with smallest surface. Further details about the implementation of such an algorithm can be found in¹⁷.

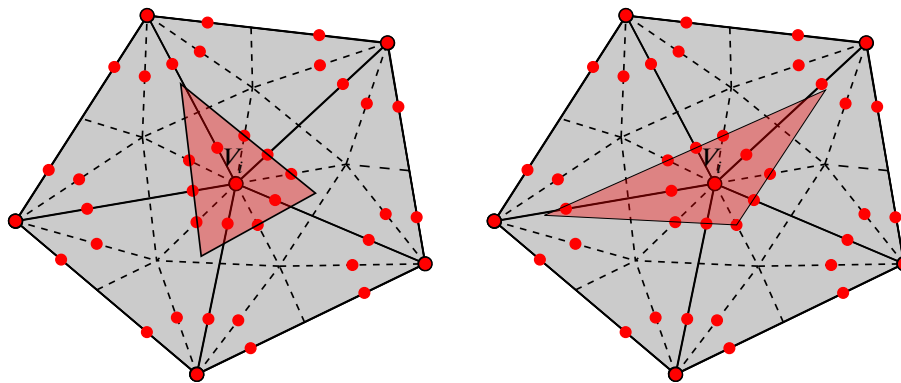


FIGURE 3 The PS-points and two possible control triangles of V_i are shown in the marked molecule Ω_i from the example triangulation Δ^* used earlier. The two control triangles are constructed by taking respectively two (left) and three edges (right) in common with the convex hull of PS_i .

Each control triangle defines three basis functions, all associated with vertex V_i and the molecule Ω_i . Therefore, the basis functions are indexed ϕ_i^q ($i = 1, \dots, n_v$, $q = 1, 2, 3$), where i indicates the vertex V_i and q the local index. Each basis function ϕ_i^q is uniquely defined by a triplet $(\alpha_i^q, \beta_i^q, \gamma_i^q)$, containing the value and gradient of ϕ_i^q in its associated vertex V_i ,

$$(\alpha_i^q, \beta_i^q, \gamma_i^q) = \left(\phi_i^q(V_i), \frac{\partial \phi_i^q}{\partial x}(V_i), \frac{\partial \phi_i^q}{\partial y}(V_i) \right). \quad (30)$$

The triplets of the three PS-spline basis functions corresponding to vertex V_i are determined from the control triangle and the position of V_i . Let the Cartesian coordinates of the control triangle vertices be $Q_i^1 = (X_i^1, Y_i^1)$, $Q_i^2 = (X_i^2, Y_i^2)$ and $Q_i^3 = (X_i^3, Y_i^3)$, and the Cartesian coordinates of $V_i = (x_i, y_i)$. The three triplets are then determined by solving

$$\begin{bmatrix} X_i^1 & X_i^2 & X_i^3 \\ Y_i^1 & Y_i^2 & Y_i^3 \\ 1 & 1 & 1 \end{bmatrix} \begin{bmatrix} \alpha_i^1 & \beta_i^1 & \gamma_i^1 \\ \alpha_i^2 & \beta_i^2 & \gamma_i^2 \\ \alpha_i^3 & \beta_i^3 & \gamma_i^3 \end{bmatrix} = \begin{bmatrix} x_i & 1 & 0 \\ y_i & 0 & 1 \\ 1 & 0 & 0 \end{bmatrix}. \quad (31)$$

The control triangle has a direct geometric interpretation for the triplet. Solving for the triplet $(\alpha_i^q, \beta_i^q, \gamma_i^q)$ of a basis function ϕ_i^q corresponds geometrically to ‘lifting’ up control triangle vertex Q_i^q of the control triangle in the z -direction and evaluating the height and gradient of the resulting plane at the location of V_i , see Figure 4.

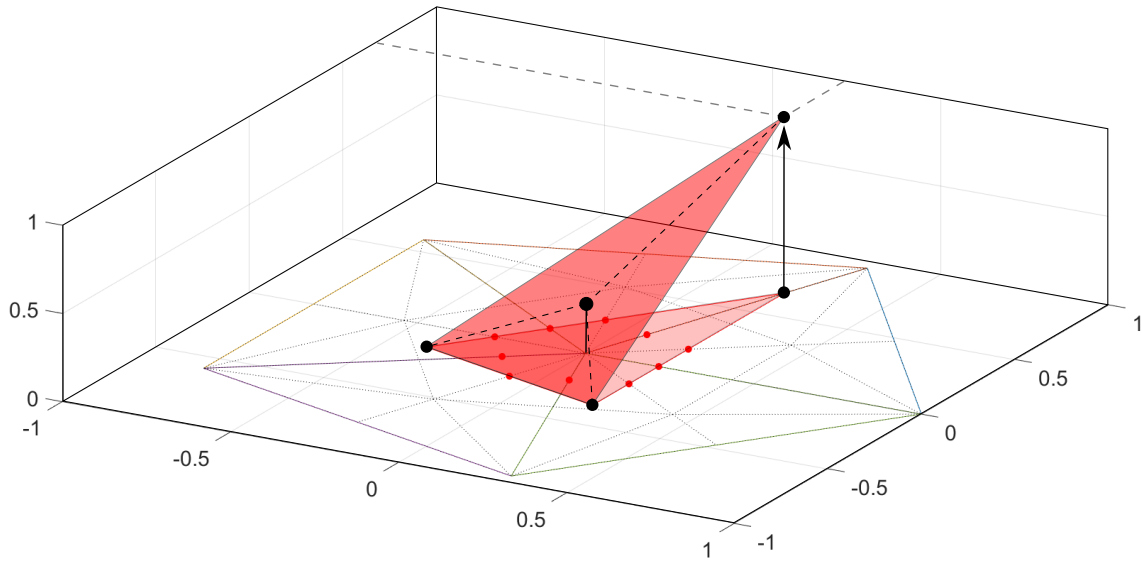


FIGURE 4 A control triangle lifted to $z = 1$ in one of its vertices for determining a triplet of a basis function. The location in the lifted plane above the vertex V_i in the middle is marked with a dot; the value and gradient there correspond to the triplet of the associated basis function.

3.3 | Bernstein-Bézier formulation for quadratic splines

From the triplet $(\alpha_i^q, \beta_i^q, \gamma_i^q)$, the PS-spline ϕ_i^q can be constructed as a piece-wise quadratic polynomial over each sub-triangle in Δ^* using barycentric coordinates. Cartesian coordinates (x, y) can be converted to barycentric coordinates (η_1, η_2, η_3) with respect to the considered triangle vertices $(x_1, y_1), (x_2, y_2), (x_3, y_3)$ as follows,

$$\begin{bmatrix} x_1 & x_2 & x_3 \\ y_1 & y_2 & y_3 \\ 1 & 1 & 1 \end{bmatrix} \begin{bmatrix} \eta_1 \\ \eta_2 \\ \eta_3 \end{bmatrix} = \begin{bmatrix} x \\ y \\ 1 \end{bmatrix}. \quad (32)$$

In Figure 5, some barycentric coordinates are shown with respect to the shown triangle.

To construct a single basis function over each sub-triangle st , 6 quadratic Bernstein polynomials $B_{i,j,k}$ are defined in barycentric coordinates,

$$B_{i,j,k}(\boldsymbol{\eta}) = \frac{2!}{i!j!k!} \eta_1^i \eta_2^j \eta_3^k, \quad \text{with } i, j, k \in \{0, 1, 2\}, \quad \text{and } i + j + k = 2, \quad (33)$$

which are non-negative and form a partition of unity. Any desired quadratic polynomial $b(\boldsymbol{\eta})$ can be uniquely constructed as a linear combination of the 6 quadratic Bernstein polynomials $B_{i,j,k}$ over a sub-triangle st ,

$$b(\boldsymbol{\eta}) = \sum_{\substack{i+j+k=2, \\ i,j,k \in \{0,1,2\}}} b_{i,j,k} B_{i,j,k}(\boldsymbol{\eta}), \quad (34)$$

where $b_{i,j,k}$ are called the Bézier ordinates. The desired quadratic polynomial can thus be fully defined by its Bézier ordinates, which can be schematically represented by associating Bézier ordinate $b_{i,j,k}$ with barycentric coordinates $\left(\frac{i}{2}, \frac{j}{2}, \frac{k}{2}\right)$, as shown in Figure 5.

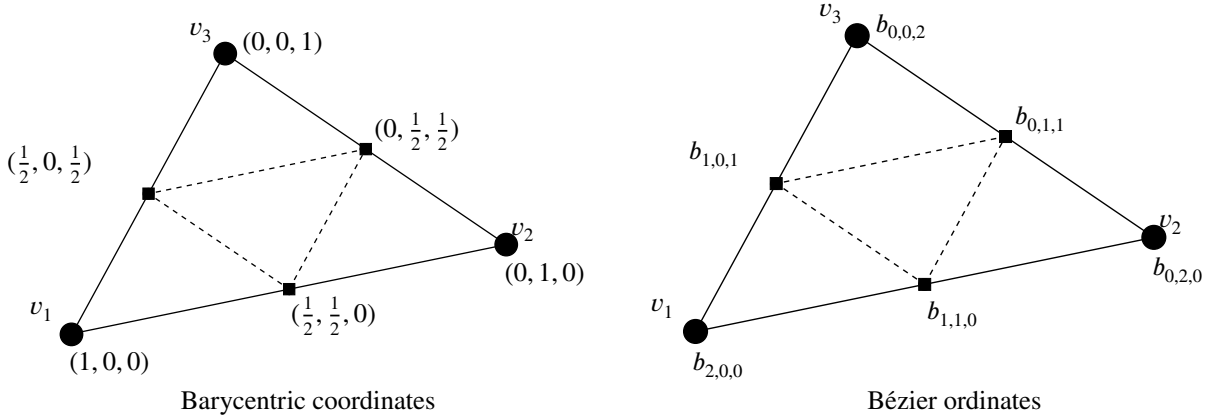


FIGURE 5 Barycentric coordinates with respect to the sub-triangle vertices (left) and the Bézier ordinates of a quadratic polynomial $b(\boldsymbol{\eta})$ (right), schematically represented at the same location.

3.4 | Construction of PS-splines

Next, consider the molecule Ω_i around a vertex V_i and one of the main-triangles t_j in the molecule, as depicted in Figure 6. The grey main-triangle has been divided into 6 sub-triangles in the refinement Δ^* . In each of the sub-triangles, the 6 locations with barycentric coordinates $\left(\frac{i}{2}, \frac{j}{2}, \frac{k}{2}\right)$, $i + j + k = 2$, $i, j, k \in \{0, 1, 2\}$ have been marked. Denote the vertices of the main-triangle by v_1 , v_2 and v_3 , with $v_1 (= V_i)$ the middle vertex of the considered molecule, and v_2 and v_3 be indexed counter-clockwise. Let the center vertex Z of the grey triangle have barycentric coordinates $Z = (a, b, c)$ with respect to vertices v_1 , v_2 and v_3 . Furthermore, let the edge vertices R have barycentric coordinates $R_{12} = (\lambda_1, \lambda_2, 0)$, $R_{23} = (0, \mu_2, \mu_3)$ and $R_{13} = (v_1, 0, v_3)$, as denoted in Figure 6. Finally, let v_1 have barycentric coordinates $v_1 = (\alpha_i^1, \alpha_i^2, \alpha_i^3)$ with respect to the control triangle vertices Q_i^1 , Q_i^2 and Q_i^3 . These values of α also correspond to the first values of the three triplets of the basis functions associated with this molecule, see Equation (31).

Finally, the three basis function ϕ_i^q , $q = 1, 2, 3$, associated with vertex V_i are defined by their Bézier ordinates on each of the triangles in the molecule around V_i . The Bézier ordinates of a basis function ϕ_i^q are shown in Figure 7. The coefficients in the figure are given in terms of the triplet $(\alpha, \beta, \gamma) = (\alpha_i^q, \beta_i^q, \gamma_i^q)$ of the considered basis function ϕ_i^q and the barycentric coordinates of $Z = (a, b, c)$, $R_{12} = (\lambda_1, \lambda_2, 0)$, $R_{13} = (v_1, 0, v_3)$, and the Cartesian coordinates of the considered triangle $v_1 = (x_1, y_1)$, $v_2 = (x_2, y_2)$ and $v_3 = (x_3, y_3)$ as follows,

$$L = \alpha + \frac{1 - \lambda_1}{2} \bar{\beta}, \quad L' = \alpha + \frac{1 - v_1}{2} \bar{\gamma}, \quad \tilde{L} = \alpha + \frac{b}{2} \bar{\beta} + \frac{c}{2} \bar{\gamma}, \quad (35)$$

with

$$\bar{\beta} = \beta(x_2 - x_1) + \gamma(y_2 - y_1) \quad \text{and} \quad \bar{\gamma} = \beta(x_3 - x_1) + \gamma(y_3 - y_1). \quad (36)$$

The three resulting PS-splines corresponding to the shown control triangle of vertex V_i are shown on the associated molecule Ω_i in Figure 8.

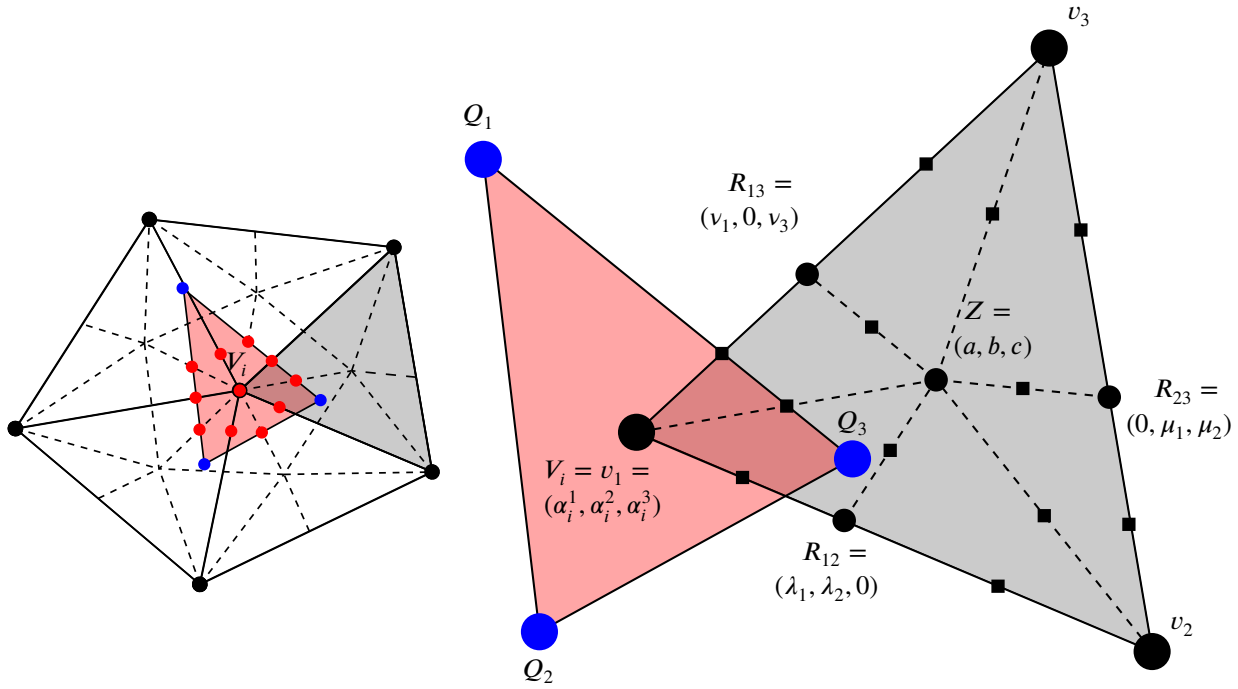


FIGURE 6 Left: the molecule around a vertex V_i . Right: one of the main-triangles in the molecule. The locations of the middle vertex Z and the edge vertices R are marked with respect to the vertices v_1, v_2 and v_3 . $v_1 (= V_i)$ is also marked with the barycentric coordinates with respect to the control triangle.

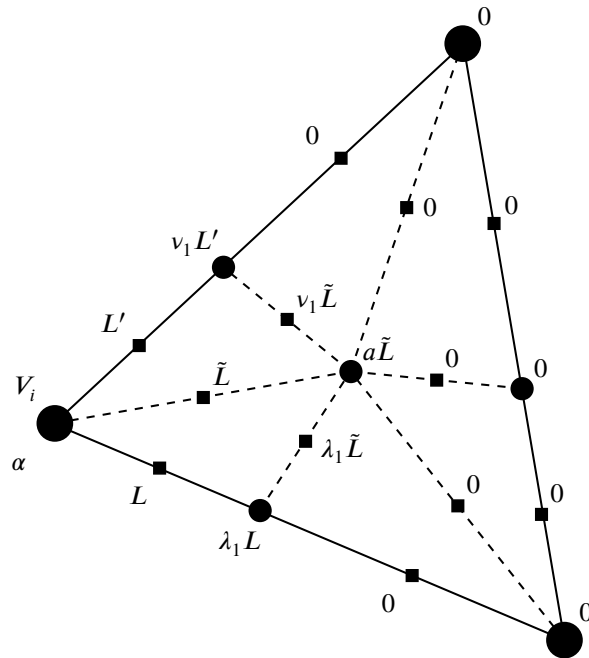


FIGURE 7 The Bézier ordinates for basis function ϕ_i^1 , corresponding to the vertex V_i considered in Figure 6. There are three different basis functions, note that for each of these basis functions, α, β and γ should correspond with the triplet $(\alpha^q, \beta^q, \gamma^q)$ corresponding to PS-triangle vertex Q_q .

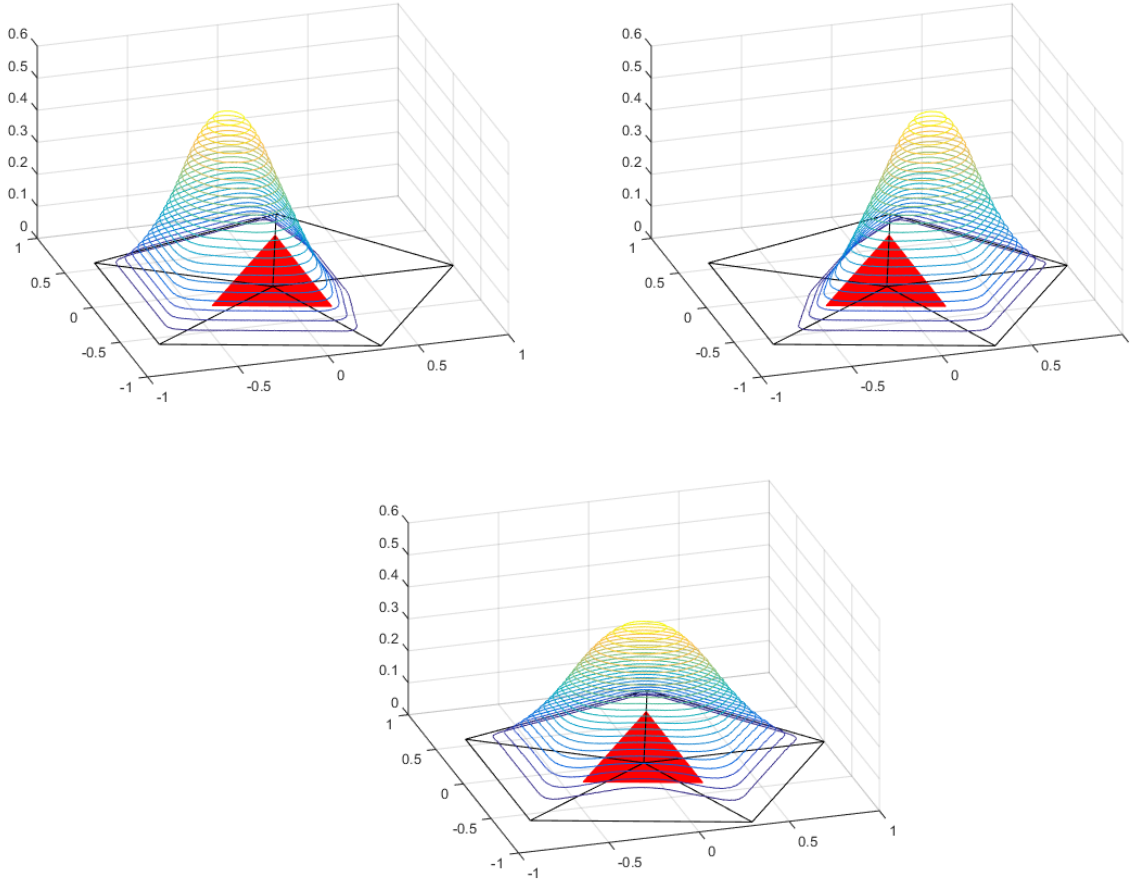


FIGURE 8 The three C^1 -continuous PS-spline basis function corresponding to the middle vertex, constructed from the marked control triangle.

3.5 | PS-splines in MPM

Throughout this paper, the resulting PS-splines are adopted as basis functions within MPM. Since each vertex is associated with three basis functions, PS-spline MPM uses three times as many basis functions compared to standard MPM for the same grid. However, the spatial function reconstruction of PS-splines is known to be of third order for smooth functions, in contrast to the second-order spatial convergence of piece-wise linear basis functions^{16,17}, so a coarser grid can be used in case of PS-splines for a comparable precision.

The basis functions can be stored per main triangle, each with nine non-zero basis functions: three basis functions ϕ_i^q , $q = 1, 2, 3$ for each of its three vertices V_i . Each of these basis functions is fully defined on this main triangle by its nine non-zero Bézier ordinates as depicted in Figure 7. The value of a basis function in a certain location \mathbf{x}^* can then be retrieved by first finding the sub-triangle in which \mathbf{x}^* is located, then finding its barycentric coordinates (η_1, η_2, η_3) with respect to that sub-triangle, and finally applying the Bernstein-Bézier formulation from Equations (33) and (34).

At the location of each boundary vertex V_i , at most three basis functions are non-zero, each of which has a known triplet describing the value and gradient at the vertex. A Dirichlet boundary condition, arising in the benchmark considered in this paper, can be applied by imposing that the value of the reconstructed field in V_i is equal to the imposed value,

$$f(V_i) = \sum_{j=1}^{n_v} \sum_{q=1}^3 c_j^q \phi_j^q(V_i) = \sum_{q=1}^3 c_i^q \phi_i^q(V_i) = \sum_{q=1}^3 c_i^q \alpha_i^q. \quad (37)$$

The Dirichlet condition can be implemented stronger, by imposing that the partial derivative tangent to the boundary in V_i is equal for the boundary condition and the reconstructed field,

$$\nabla f(V_i) \cdot \hat{\mathbf{r}}(V_i) = \sum_{q=1}^3 c_i^q \nabla \phi_i^q \cdot \hat{\mathbf{r}} = \sum_{q=1}^3 c_i^q (\beta_i^q \hat{\mathbf{r}}_x + \gamma_i^q \hat{\mathbf{r}}_y), \quad (38)$$

where $\hat{\mathbf{r}}$ is the tangent to the boundary.

4 | NUMERICAL RESULTS

To assess the quality of the proposed PS-MPM, a two-dimensional benchmark is considered. Throughout this section, the performance of PS-MPM with respect to the grid-crossing error and the order of spatial convergence is compared with standard MPM.

4.1 | Vibrating plate undergoing axis-aligned displacement

A Neo-Hookean vibrating plate on the unit square is considered. The plate undergoes axis-aligned displacement that allows to construct the analytic solution using the method of manufactured solutions (MMS): the analytic solution is assumed *a priori*, and the corresponding body force is calculated accordingly and imposed. This benchmark has been adopted from¹⁸. Using the material properties from Table 1, the desired analytic solution for displacement is given by

$$u_x = u_0 \sin(2\pi x) \sin\left(\sqrt{(E/\rho_0)} \pi t\right), \quad (39)$$

$$u_y = u_0 \sin(2\pi y) \sin\left(\sqrt{(E/\rho_0)} \pi t + \pi\right), \quad (40)$$

The corresponding body forces¹⁸ are

$$g_x = \pi^2 u_x \left(\frac{4\mu}{\rho_0} - \frac{E}{\rho_0} - 4 \frac{\lambda [\ln(D_{xx} D_{yy}) - 1] - \mu}{\rho_0 D_{xx}^2} \right), \quad (41)$$

$$g_y = \pi^2 u_y \left(\frac{4\mu}{\rho_0} - \frac{E}{\rho_0} - 4 \frac{\lambda [\ln(D_{xx} D_{yy}) - 1] - \mu}{\rho_0 D_{yy}^2} \right), \quad (42)$$

in which the Lamé constant λ , the shear modulus μ , and the normal components of the deformation gradient D_{xx} and D_{yy} are defined as

$$\lambda = \frac{E\nu}{(1+\nu)(1-2\nu)}, \quad \mu = \frac{E}{2(1+\nu)}, \quad (43)$$

$$D_{xx} = 1 + 2u_0 \pi \cos(2\pi x) \sin\left(\sqrt{(E/\rho_0)} \pi t\right), \quad (44)$$

$$D_{yy} = 1 + 2u_0 \pi \cos(2\pi y) \sin\left(\sqrt{(E/\rho_0)} \pi t + \pi\right). \quad (45)$$

TABLE 1 The parameters of the considered vibrating plate benchmark.

Quantity	Symbol	Value	Unit
Initial density	ρ_0	10^3	[kg/m ³]
Young's modulus	E	10^7	[Pa]
Poisson's Ratio	ν	0.3	[—]
Length	L	1	[m]
Width	H	1	[m]
Maximum displacement	u_0	0.05	[m]

This benchmark was simulated using standard MPM and PS-MPM. For both cases, the particle stresses and the spatial convergence rate for the displacement were determined. An unstructured triangular grid was used for discretisation with material points initialised in equally spaced rows and columns, as shown in Figure 9. A time step size of $\Delta t = 0.18 \frac{h}{C}$ was chosen, where h is the typical length of a triangle edge and $C = \sqrt{E/\rho_0}$ is the thin bar wave speed. For the adopted parameters, the imposed solution in Equation (39)-(40) has period of $T = 0.02$ seconds.

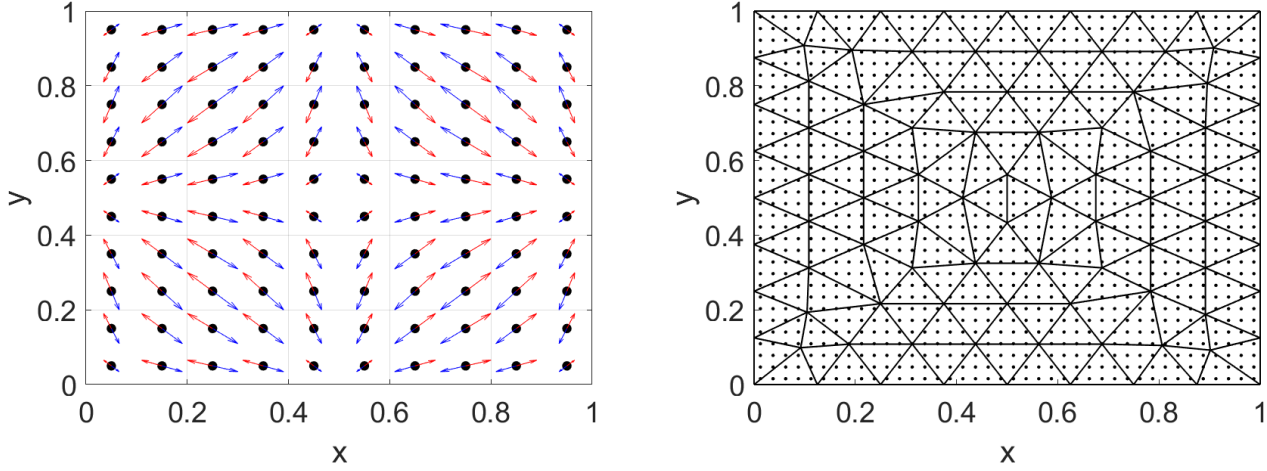


FIGURE 9 A unit square for simulating axis-aligned displacement. Left: in the exact solution, particles (marked with dots) move back and forth along the marked vectors. Right: an unstructured grid with $h = 1/8$ with particles initially in square configuration.

4.2 | Grid-crossing error comparison

Figure 10 displays the normal stress field for the x -direction, obtained with standard MPM and PS-MPM with a comparable number of basis functions and material points on an unstructured grid. The configuration for standard MPM used 289 basis functions ($h = 1/16$) and 20.480 material points (40 particles per element), whereas PS-MPM was used with 243 basis functions ($h = 1/8$) and 23.040 material points (180 particles per element). While the stress field for PS-MPM can not be distinguished from the exact solution by sight, the solution for standard MPM shows oscillatory behaviour for individual particles over time, resulting in an irregular stress field. The use of more particles and basis functions within standard MPM leads to a stress field that converges to the analytic solution on average. However, this makes the standard MPM computationally more expensive.

Furthermore, individual particle stresses are not guaranteed to converge, showing a relative error of up to 1 at places where grid-crossing occurs. To illustrate this, the stress and movement of a single particle over time, obtained with standard MPM and PS-MPM, is shown in Figure 11. At $t = 0$, the particle is positioned at $(x, y) \approx (0.25, 0.47)$ and starts moving in the positive x - and negative y -direction. For standard MPM and PS-MPM, an unstructured grid with a typical edge length of $h = 1/8$ and $h = 1/4$ is used, respectively. This results in 92 piece-wise linear and 90 PS-spline basis functions. For both methods, a total of 5120 particles was used.

With standard MPM, the stress shows oscillations and deviates from the exact solution over time. The stress obtained with PS-MPM is smooth and more accurate. The movement obtained with PS-MPM shows no oscillations, in contrast to the movement obtained with standard MPM, and is in closer agreement with the exact solution.

4.3 | Spatial convergence

To compare both methods qualitatively, the root-mean-squared (RMS) error is used,

$$E(t) = \sqrt{\frac{\sum_{i=1}^{n_t} \sum_{p=1}^{n_p} (x_p(t_i) - \hat{x}_p(t_i))^2}{n_p n_t}}, \quad (46)$$

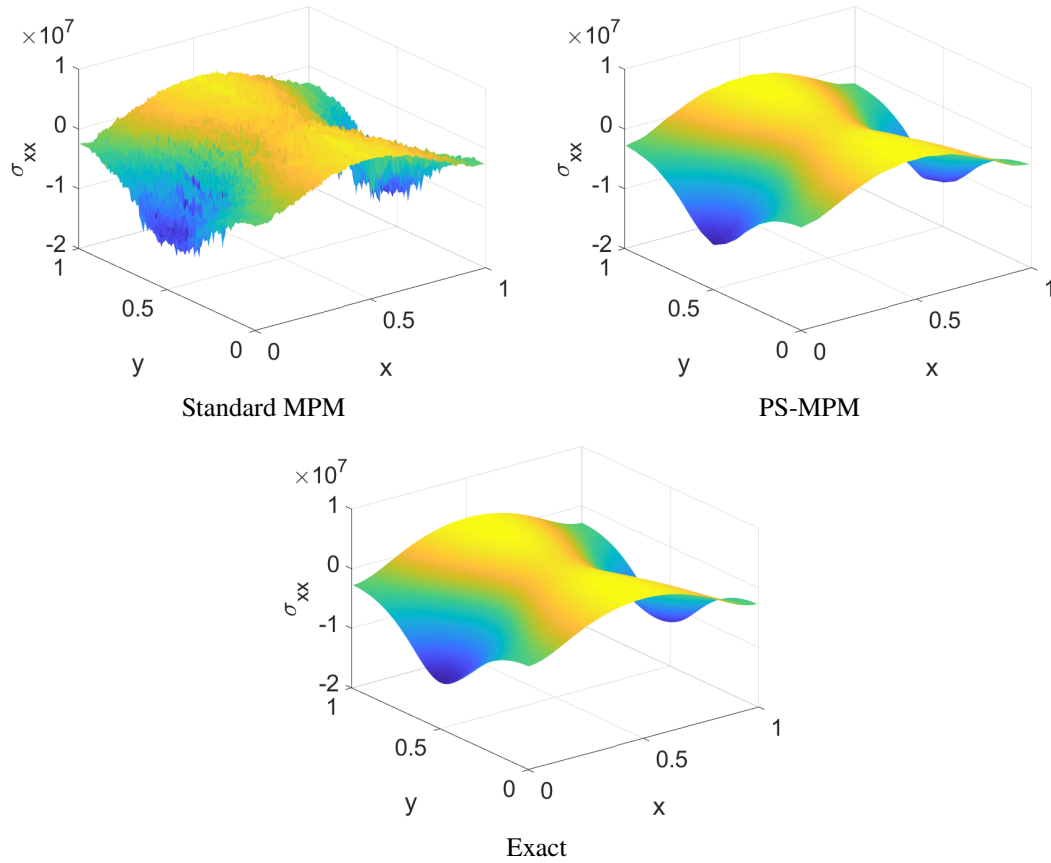


FIGURE 10 The normal stress in the x -direction at $t = 0.016$ s.

in which the average is taken of the squared error in each particle at each time step, for all n_p particles and all n_t time steps. This error is normalised for the number of particles and time steps, which allows a fair comparison of simulations with varying numbers of data points. For the results in the remainder of this section, all particles are considered for all time steps in a single period. The spatial convergence of standard MPM and PS-MPM is determined by varying the typical edge length h , under the assumption that the spatial error is much larger than the numerical quadrature integration error (see Equations (13)-(15)) and time-stepping error. It has been observed that the time-integration error is indeed sufficiently small, but the required number of particles needed for a sufficiently accurate integration increases rapidly as h decreases.

Figure 12 shows the spatial convergence of both standard MPM and PS-MPM for different numbers of particles per element on an unstructured grid. When a sufficient number of particles is adopted, standard MPM shows second-order spatial convergence, whereas PS-MPM converges with third order. Furthermore, the RMS-error is smaller with PS-MPM for all considered configurations. In order to achieve the optimal convergence order for both standard MPM and PS-MPM, the number of integration particles required increases rapidly. Figure 12 also shows the integration error as a function of the number of particles. The convergence rate in the number of particles is measured to be of only first order. The inaccurate integration in MPM due to the use of particles as integration points is known to limit the spatial convergence. Over the years, different measures have been proposed to decrease the quadrature error in MPM based on function reconstruction techniques like MLS⁴, cubic splines⁷ and Taylor Least Squares¹⁹. The combination of PS-MPM with function reconstruction techniques to obtain optimal convergence rates with a moderate number of particles is subject to future research to make PS-MPM attractive for practical applications. Furthermore, the situation of partially-empty elements will be investigated in more depth, which may lead to stability problems due to an ill-conditioned mass matrix², which is a common problem of the MPM⁵.

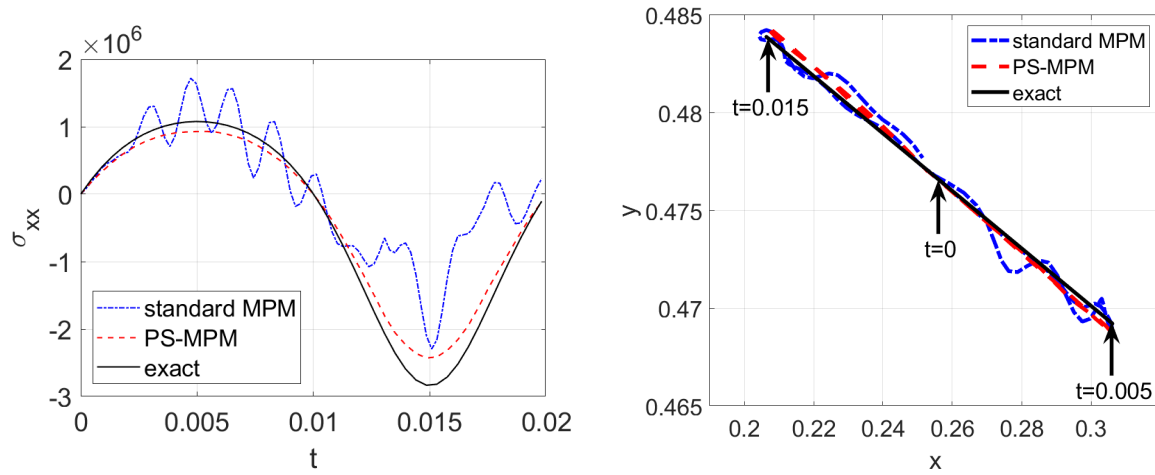


FIGURE 11 Stress and movement of a single particle over time.

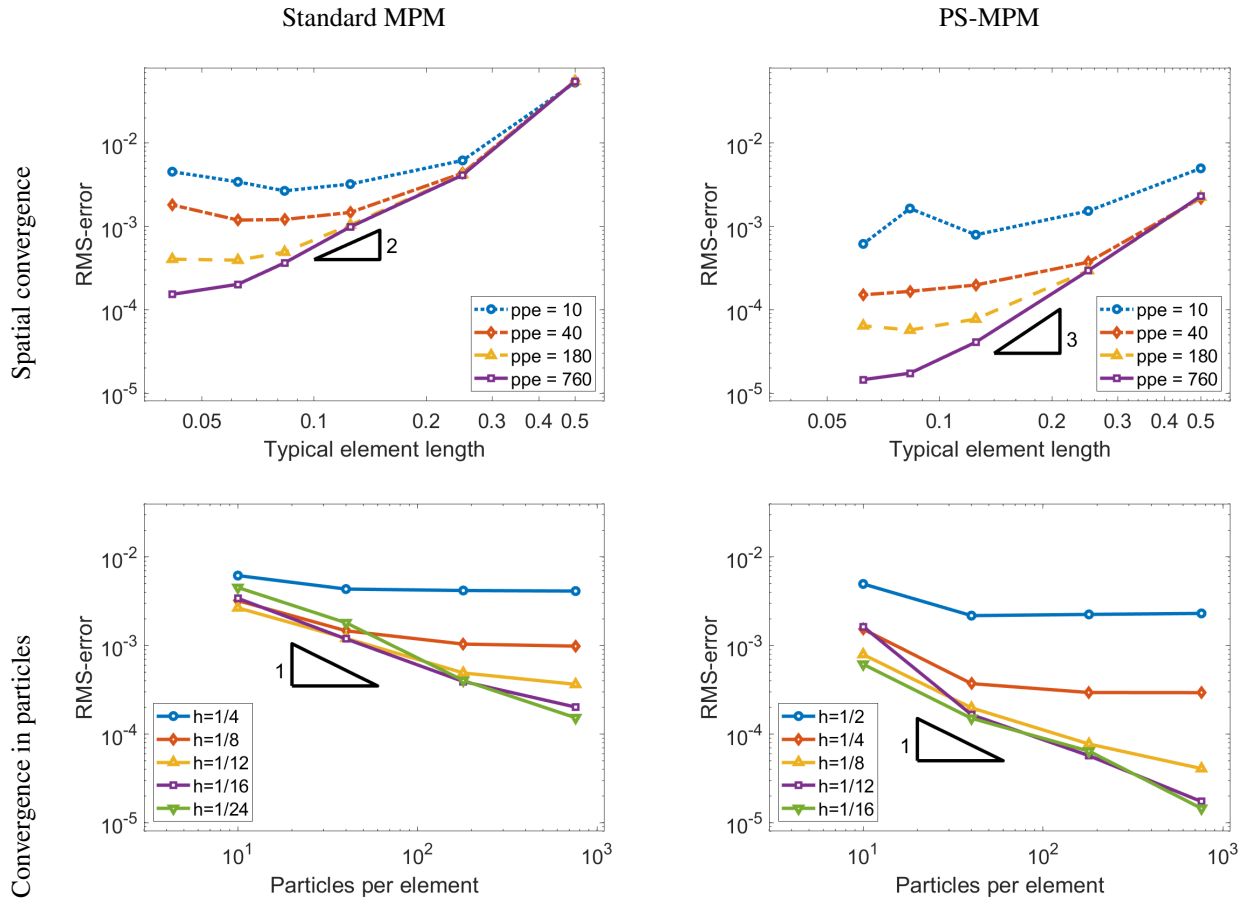


FIGURE 12 Spatial convergence (top) and convergence in the number of particles per element (bottom) for both standard MPM (left) and PS-MPM (right).

5 | CONCLUSION

In this paper, we presented an MPM for unstructured triangulations using piece-wise quadratic C^1 -continuous Powell-Sabin spline basis functions. PS-MPM leads to a mathematically sound method to eliminate grid-crossing errors and improve the spatial convergence compared to standard MPM. Numerical results show that the smooth gradients of PS-splines eliminate grid-crossing errors and render good results for the particle stresses. Furthermore, particle displacements are captured better compared to standard MPM and higher-order spatial convergence rates can be obtained.

ACKNOWLEDGEMENTS

We thank Dr. V. Galavi from the Dutch research institute Deltares for his comments and contribution in this work. Funding support provided by Deltares is also gratefully acknowledged.

References

1. Sulsky D, Schreyer H, Peterson K, Kwok R, Coon M. Using the material point method to model sea ice dynamics. *Journal of Geophysical Research* 2007; 76: 922–948.
2. Kafaji IKa. *Formulation of a dynamic material point method (MPM) for geomechanical problems*. PhD thesis. Universität Stuttgart, 2013.
3. Andersen S, Andersen L. Modelling of landslides with the material-point method. *Computational Geosciences* 2010; 14: 137–147.
4. Gong M. *Improving the Material Point Method*. The University of New Mexico . 2015.
5. Sulsky D, Chen Z, Schreyer HL. A particle method for history-dependent materials. *Computer Methods in Applied Mechanics and Engineering* 1994; 118(1-2): 179–196.
6. Bardenhagen S, Kober E. The generalized interpolation material point method. *Computer Modeling in Engineering and Sciences* 2004; 5(6): 477–496.
7. Tielen R, Wobbes E, Möller M, Beuth L. A high order material point method. *Procedia Engineering* 2017; 175: 265–272.
8. Steffen M, Kirby RM, Berzins M. Analysis and reduction of quadrature errors in the material point method (MPM). *International Journal for Numerical Methods in Engineering* 2008; 76(6): 922–948.
9. Tielen R. High-order Material Point Method. Master's thesis. Delft University of Technology. 2016.
10. Zhang DZ, Ma X, Giguere PT. Material point method enhanced by modified gradient of shape function. *Journal of Computational Physics* 2011; 230(16): 6379–6398.
11. Gan Y, Sun Z, Chen Z, Zhang X, Y L. Enhancement of the material point method using B-spline basis functions. *International Journal for Numerical Methods in Engineering* 2017; 113: 411–431.
12. Cromer A. Stable solutions using the Euler approximation. *American Journal of Physics* 1981; 49(5): 455–459.
13. Dierckx P, Van Leemput S, Vermeire T. Algorithms for surface fitting using Powell-Sabin splines. *IMA Journal of numerical analysis* 1992; 12(2): 271–299.
14. Dierckx P. On calculating normalized Powell-Sabin B-splines. *Computer Aided Geometric Design* 1997; 15(1): 61–78.
15. Powell MJ, Sabin MA. Piecewise quadratic approximations on triangles. *ACM Transactions on Mathematical Software (TOMS)* 1977; 3(4): 316–325.

16. Speleers H, Manni C, Pelosi F, Sampoli ML. Isogeometric analysis with Powell–Sabin splines for advection–diffusion–reaction problems. *Computer Methods in Applied Mechanics and Engineering* 2012; 221: 132–148.
17. De Koster P. Towards a Material Point Method with Powell-Sabin spline basis functions. Master's thesis. Delft University of Technology. 2018.
18. Sadeghirad A, Brannon RM, Burghardt J. A convected particle domain interpolation technique to extend applicability of the material point method for problems involving massive deformations. *International Journal for Numerical Methods in Engineering* 2011; 86(12): 1435–1456.
19. Wobbes E, Möller M, Galavi V, Vuik C. Conservative Taylor least squares reconstruction with application to material point methods. *International Journal for Numerical Methods in Engineering* 2019; 117(3): 271–290.

